Chaos

Wave chaos enhanced light trapping in optically thin solar cells

E. Seim, A. Kohler, R. Lukacs, M. A. Brandsrud, E. S. Marstein, E. Olsen, and R. Blümel

open access

View Online   Export Citation   CrossMark

ARTICLES YOU MAY BE INTERESTED IN

Chaos: From theory to applications for the 80th birthday of Otto E. Rössler
Chaos: An Interdisciplinary Journal of Nonlinear Science **31**, 060402 (2021); https://doi.org/10.1063/5.0058332

NetworkDynamics.jl—Composing and simulating complex networks in Julia
Chaos: An Interdisciplinary Journal of Nonlinear Science **31**, 063133 (2021); https://doi.org/10.1063/5.0051387

Artificial radio lighting with sources of microwave dynamic chaos
Chaos: An Interdisciplinary Journal of Nonlinear Science **31**, 063135 (2021); https://doi.org/10.1063/5.0053504

Scilight
Summaries of the latest breakthroughs in the physical sciences

AIP Publishing

Wave chaos enhanced light trapping in optically thin solar cells

E. Seim,[1,a] (iD) A. Kohler,[1] R. Lukacs,[2] M. A. Brandsrud,[1] E. S. Marstein,[3,4] E. Olsen,[1] and R. Blümel[5]

AFFILIATIONS

[1] RealTek, Norwegian University of Life Sciences, Ås 1430, Norway
[2] The Norwegian Public Service Pension Fund, Oslo 0212, Norway
[3] Department of Solar Energy, Institute of Energy Technology, Kjeller 2007, Norway
[4] Department of Technology Systems, University of Oslo, Oslo 0371, Norway
[5] Department of Physics, Wesleyan University, Middletown, Connecticut 06459-0155, USA

[a] **Author to whom correspondence should be addressed:** e.seim.es@gmail.com

ABSTRACT

Enhancing the energy output of solar cells increases their competitiveness as a source of energy. Producing thinner solar cells is attractive, but a thin absorbing layer demands excellent light management in order to keep transmission- and reflection-related losses of incident photons at a minimum. We maximize absorption by trapping light rays to make the mean average path length in the absorber as long as possible. In chaotic scattering systems, there are ray trajectories with very long lifetimes. In this paper, we investigate the scattering dynamics of waves in a model system using principles from the field of quantum chaotic scattering. We quantitatively find that the transition from regular to chaotic scattering dynamics correlates with the enhancement of the absorption cross section and propose the use of an autocorrelation function to assess the average path length of rays as a possible way to verify the light-trapping efficiency experimentally.

Classical chaotic scattering leads to trapped rays with long lifetimes, which are of importance in improving light management for more efficient solar cells. In this paper, we study the wave dynamics in solar-cell models with proven chaotic dynamics on the classical level. We show a connection between the emergence of wave chaos and the enhancement of absorption efficiency due to light trapping.

I. INTRODUCTION

The demand for renewable energy is driven by the need for producing clean energy to meet climate and sustainability goals. Photovoltaic solar cells are a rapidly growing technology that has resulted in a tremendous increase in photovoltaics (PV) energy production over the last decade. From 2010 to 2018, the world-wide total installed capacity increased more than tenfold from $40\,\mathrm{GW_P}$ to over $500\,\mathrm{GW_P}$.[1] The share of PV is now 2.6% of the total electricity generated globally and covers 4.3% of European energy demand. To become even more competitive, the price per $\mathrm{GW_P}$ needs to be

lowered. The efficiency of solar cells is the most important metric to improve in this regard. Single-junction silicon-based technology is by far the most commonly used technology today. This technology has matured to the point that the theoretical Shockley–Queisser limit of 29% is almost realized[2,3] as shown by the demonstrated PV cell record for a crystalline Si of 26.7%.[4,5] However, producing thin solar cells reduces the cost and environmental footprint at the expense of efficiency since the absorbing layer is less likely to absorb light than a thicker cell would, and, in the case of silicon, the indirect bandgap makes the material a weak absorber. To mitigate the losses from creating thinner solar cells, smart management of light is required. If the incoming light is effectively trapped within a solar cell, the transmission and reflection losses are minimized, thus maximizing the efficiency. Moreover, thinner solar cells entail additional benefits by being less prone to bulk recombination and having better voltage characteristics.

The concept of light trapping is often analyzed from the perspective of geometric optics. The goal is to force photons from the incoming sunlight into rays that stay long enough in the absorbing layer of the solar cell to excite electrons and holes. To achieve

long-lived ray trajectories, one must control the dynamics of the incoming light rays. In general, improved light trapping is engineered by creating or adding structures or textures. They can be on the surface and on the back side of the solar cell, or they may be realized as advanced plasmonic structures.[6–13]

Solar cells are ray-splitting systems since the surface of the solar cells acts as a ray-splitting boundary where rays are reflected or transmitted according to probabilities given by the Fresnel equations.[14] Ray-splitting dynamics has been studied extensively in the context of chaotic scattering,[15–18] in which ray splitting[19–25] and ray trapping[26,27] play a major role. Both concepts are of central relevance to light trapping in solar-cell applications. Ray trapping is connected to the defining property of a system exhibiting chaotic dynamics, which is the hypersensitivity to initial conditions. The presence of chaotic dynamics has interesting implications in the context of absorption in solar cells. Bunimovich showed that dynamics in a Bunimovich billiard, a bounded dynamical system, is ergodic,[28,29] meaning that the whole energetically accessible phase space of the system is visited by a generic ray, i.e., a ray started with initial conditions that are not too special. If ergodic rays are present in a solar cell, it means that incoming rays are deflected away from the vertical direction, resulting in a longer average path length.[30] There are few reports of the benefits of chaotic scattering dynamics in solar cells. Mariano et al.[31] report experimental and computational findings that a solar cell integrated on a special photonic fiber plate leads to an optically ergodic system and a greatly enhanced light absorption. Using classical ray-tracing calculations and verifying the results with a commercial finite-difference time-domain (FDTD) solver, Seim et al.[32] recently showed that the transition from regular to chaotic scattering dynamics correlates with the enhancement of the absorption efficiency. The result was proven for a model system with a shape akin to a Bunimovich billiard, where the transition from regular to chaotic scattering was controlled by a single parameter. It was also shown that the result was structurally stable; i.e., it was not sensitive with respect to the system parameters chosen. This is a very important property for the successful technical realization of such a system. If the phenomenon was only valid for a special, exactly realized shape, one could never expect to be able to reproduce the shape in the lab, let alone in a large-scale industrial process.

While in systems of any dimension, geometrical ray optics and electromagnetic (E&M) wave simulations produce comparable results in the short wavelength limit, in two or more dimensions, there is not a general ray theory known to the authors that is exact for systems that cannot be considered to be within the geometrical optics limit. However, in effectively one-dimensional systems, for instance, a stack of planar films, an exact ray theory exists.[33] In higher-dimensional systems, we are, therefore, in need of E&M wave calculations for simulating optical systems and obtaining their optical properties accurately. A solar cell is an inherently wave-mechanical scattering system. In terms of scattering dynamics, the dynamics on the wave level "feel" the underlying classical dynamics,[17] but chaos on the classical level does not necessarily imply chaos on the wave level, more commonly called *wave chaos*. The aim of this paper is to confirm the findings of Seim et al.[32] by applying techniques from the fields of quantum and wave chaos to extend our knowledge of how chaos can

improve the light-trapping properties in surface-structured solar cells.

We start out by presenting a very brief account of the aspects of classical and quantum chaos that are relevant in the context of this paper, enhancing the light trapping in solar cells. Section III explains the model system and the numerical methods used. Then, the results are presented in two parts, the first highlights the appearance of chaotic signatures and the enhancement of the absorption efficiency as an effect of varying a system parameter. The second part shows that these effects are tied to the transition from the regular to chaotic scattering regime. The results and usefulness to light trapping are summarized in Sec. IV.

II. CLASSICAL AND QUANTUM CHAOS

Chaos is a phenomenon that is seen in many dynamical systems. The defining trait of chaotic systems is that the dynamical motion is strongly dependent on the initial conditions. Chaos is divided into two separate, but connected fields, classical chaos and wave chaos.

A. Classical chaos

Classical chaos started with Jacques Hadamard in 1898 with his study of exponential divergence of rays in a dynamical billiard. The rays in dynamical billiards are the trajectories they trace out as particles move on a surface bounded by reflecting walls. Dynamical billiards are, therefore, closed systems. Various closed systems with chaotic dynamics have been studied in great detail, with perhaps most extensively studied being the Sinai and Bunimovich billiards.[34,35] The open counterpart to bounded billiard systems are called scattering systems.[16] Classical chaos in ray systems is often characterized by how two rays with very similar initial conditions separate from each other in the phase space as a function of time. In regular systems without chaos, the separation is linear in time, while in irregular chaotic systems, the separation is exponential. The Lyapunov exponent λ gives the rate of divergence

$$s(t) = e^{\lambda t} s(0), \qquad (1)$$

where $s(0)$ is the initial separation distance and $s(t)$ is the separation at a time t. A positive Lyapunov exponent is needed for exponential divergence and is, therefore, used as a tool to diagnose chaos in a system.

B. Quantum chaos

Quantum chaos, or more generally wave chaos, is a dynamical phenomenon that may occur quite generally in all wave systems. Wave chaos can appear in real, complex, as well as vector fields, and the governing wave equations can be linear equations such as the Schrödinger equation or Maxwell's equations, or they can be non-linear such as the Gross–Pitaevskii equation.[36]

In 1955, Wigner introduced random matrices to model the spectra of heavy atomic nuclei,[37,38] a tool that has since proven enormously useful in analyzing wave chaos.[36] Random matrix theory, in particular, with a view on its application to wave chaos, was then developed further by Dyson, Mehta, and others.[36,39] One of the central results is the Wigner surmise. It postulates the probability

density function, $P(s)$, of a sequence of nearest-neighbor spacings between energy levels in heavy nuclei. It is given by

$$P(s) = \frac{\pi s}{2} e^{-\pi s^2/4}, \qquad (2)$$

where $s = s'/D$ with s' being a particular nearest-neighbor spacing and D being the mean distance between neighboring energy levels. Equation (2) is commonly referred to as the Wigner surmise or the Wigner distribution. The class of random matrices that this particular version of the Wigner distribution is universal for is called the Gaussian orthogonal ensemble (GOE).[40,41] Later, it was conjectured by Bohigas *et al.* that all chaotic systems have the universality of the Wigner distribution predicted by random matrix theory.[42] Confidence in the conjecture was built over the years by a large amount of evidence.[36,39,43] It is generally agreed upon that (generic) regular systems have Poissonian level distributions[44–46] and that (generic, time-reversal invariant) chaotic systems have level distributions fitting the Wigner surmise.[42,47,48]

The transition from regular to chaotic dynamics has been studied in the context of universality in the S-matrix fluctuations.[44,49] Berry and Robnik,[50] and Brody[51,52] have developed models to make quantitative predictions for the level statistics as a system gradually becomes more irregular. These models are interpolations between the Poisson and Wigner distributions. The Berry–Robnik distribution is

$$P_{BR}(S, \rho) = \rho^2 e^{-\rho S}\mathrm{erfc}(\sqrt{\pi}\,\bar{\rho}S/2)$$
$$+ (2\rho\bar{\rho} + \pi\bar{\rho}^3 S/2)\, e^{-\rho S - \pi\bar{\rho}^2 S^2/4}, \qquad (3)$$

where $\bar{\rho} = 1 - \rho$ is the fraction of chaos in the available phase space. Brody's distribution is

$$P_B(S, \omega) = \alpha(\omega + 1)S^\omega\, e^{-\alpha S^{\omega+1}}, \qquad (4)$$

where

$$\alpha = \left[\Gamma\left(\frac{\omega + 2}{\omega + 1}\right)\right]^{\omega+1} \qquad (5)$$

and ω is a measure of the level repulsion. Thus, $\omega = 0$ yields the Poisson distribution, and $\omega = 1$ yields the Wigner surmise. However, the ω in the Brody distribution does not have a rigorous physical interpretation like the ρ has in the Berry–Robnik distribution. We use these distributions later on as tools to quantify the onset of chaos in a model system by comparing them to histograms of level statistics.

III. THE FILM+DOME SYSTEM

The model system shown in Fig. 1(a) is a scattering system. It is comprised of three mirrors arranged like a bucket (left, bottom, and right), while the system is open at the top, where it has a non-absorbing dome structure placed on top of a light-absorbing film. Thus, in the context of electromagnetic theory and optics, our system, conceptually, is a waveguide,[53] closed at one end, with a dielectric coupling structure, i.e., the dielectric dome, attached to its open end. Both structures, i.e., film and dome, are characterized by their index of refraction, $n_{\mathrm{film}} \in \mathbb{C}$ and $n_{\mathrm{dome}} \in \mathbb{R}$, respectively. We call this the film+dome system. Because our aim is to study the
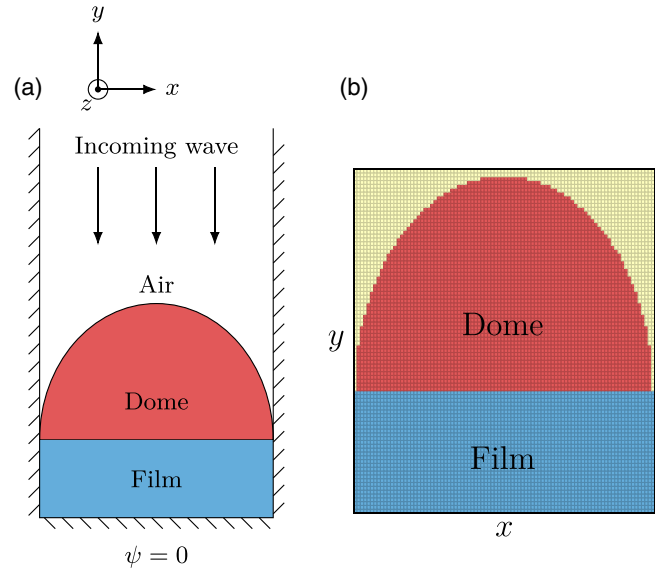

FIG. 1. (a) The film+dome scattering system is enclosed in a mirror-shaped bucket. (b) The discretized film+dome system.

effects of wave chaos in an optically thin surface-structured solar cell, we model the absorption capabilities of the solar cell by the imaginary part of the index of refraction alone, without any additional device modeling. Thus, the approach chosen is well suited to study scattering phenomena. The aim is not to predict the I–V characteristics of an experimental realization of the same system. We have previously investigated the classical dynamics of the same system.[32]

The scattering problem depicted in Fig. 1(a) is two-dimensional but equivalent to the three-dimensional problem where the structure is extended out of the two-dimensional plane of the picture; i.e., we assume cylindrical symmetry along the z axis. In this geometry, it is convenient to assume that the polarization of the incoming radiation is pointing along the z direction of the extended structure since this allows for a two-dimensional description of the associated E&M wave problem. As a consequence of this assumption, the polarization is always perpendicular to the plane of incidence. In this case, the E&M wave equation is the Helmholtz equation. It is interesting to note that the problem is completely analogous to the time-independent Schrödinger equation if the solutions are assumed to be separable in time and space. We solve the Helmholtz equation to get the steady state solutions of the scattering problem,

$$(\nabla^2 + n^2 K^2)\psi = 0, \qquad (6)$$

where n is the complex index of refraction in the two-dimensional region enclosed by the mirrors, $x \in [0, w]$ and $y \in [0, \infty]$. We opt to solve the Helmholtz equation by using Green's function method. Green's function, $G(x, x', y, y'; K)$, obeys the boundary conditions

$$\psi(x, 0) = 0, \qquad (7a)$$

$$\psi(0, y) = \psi(w, y) = 0 \qquad (7b)$$

and is thus constructed by the normalized eigenfunctions

$$\phi_{mk}(x,y) = \frac{2}{\sqrt{\pi w}} \sin\left(\frac{m\pi x}{w}\right) \sin(ky), \qquad (8)$$

where $k \in \mathbb{R}$, and $m \in \mathbb{N}$, according to the waveguide interpretation of our system above, is the waveguide mode index. $G(x,x',y,y';K)$ is now constructed according to

$$G(x,x',y,y';K) = \sum_{m=-\infty}^{\infty} \int_0^\infty \frac{\phi_{mk}(x,y)\phi_{mk}(x',y')\,\mathrm{d}k}{K^2 - \frac{\pi^2 m^2}{w^2} - k^2}, \qquad (9)$$

where the sum is over all modes, m, of the system (waveguide), including both propagating modes and evanescent modes. The full derivation of $G(x,x',y,y';K)$ can be found in Appendix A. Depending on whether K is real (propagating mode) or complex (evanescent mode), we split $G(x,x',y,y';K)$ into two branches, corresponding to propagating and evanescent modes, according to

$$K^2 - \frac{\pi^2 m^2}{w^2} > 0, \quad \text{propagating modes}, \qquad (10)$$

$$K^2 - \frac{\pi^2 m^2}{w^2} < 0, \quad \text{evanescent modes}, \qquad (11)$$

respectively. The complete Green's function is divided into two expressions

$$G_{prop} = \sum_{m=1}^{M} \frac{i}{wB_m} \sin\left(\frac{m\pi x}{w}\right) \sin\left(\frac{m\pi x'}{w}\right) \times \left[e^{iB_m(y+y')} - e^{iB_m|y-y'|}\right], \qquad (12)$$

$$G_{eva} = \sum_{m=M+1}^{\infty} \frac{1}{wA_m} \sin\left(\frac{m\pi x}{w}\right) \sin\left(\frac{m\pi x'}{w}\right) \times \left[e^{-A_m(y+y')} - e^{-A_m|y-y'|}\right], \qquad (13)$$

with $A_m = \sqrt{\frac{\pi^2 m^2}{w^2} - K^2}$, $B_m = \sqrt{K^2 - \frac{\pi^2 m^2}{w^2}}$, and M is the number of propagating modes available given by the floor function

$$M = \left\lfloor \frac{Kw}{\pi} \right\rfloor. \qquad (14)$$

The allowed incoming waves are plane waves traveling along the y axis in the negative direction, weighted by a sine function in the x-direction. They are of the form

$$\psi_{in} = e^{-ik_y y} \sin(k_x x), \qquad (15)$$

where $k_x = p\pi/w$ and p is a positive integer. For each value of p, there is a propagating mode associated with an incoming wave. The wavelength λ of the incoming wave is given by $k_y = 2\pi/\lambda$, and K is defined in relation to k_y and k_x in the following way:

$$K^2 = k_y^2 + k_x^2. \qquad (16)$$

Three film+dome systems were evaluated in order to ensure that the results are not dependent on special system parameters, i.e., to ensure structural stability. In order to make contact with the parameter settings in Ref. 32, which allows us to corroborate the classical

results therein with detailed electromagnetic wave simulations, the three film+dome systems investigated here consist of a $5\,\mu$m wide absorbing film with index of refraction $n_{\text{film}} = 2 + 0.0054i$. The three films are 1, 2, and $3\,\mu$m thick, while the dome is $3.46\,\mu$m tall and $5\,\mu$m wide. The index of refraction in the dome, n_{dome}, is the variable parameter.

A. Absorption cross section

The solution of the non-free Helmholtz equation can be found using the Lippmann–Schwinger formula

$$\psi_p(x,y) = \phi_p(x,y) - \int G(K,x,x',y,y')K^2$$
$$\times \left[1 - n(x',y')^2\right]\psi_p(x',y')\,\mathrm{d}x'\,\mathrm{d}y', \qquad (17)$$

where $\phi_p(x,y)$ is one of the M free solutions, meaning no dielectric material in the bucket-shaped mirror configuration. The free solution for each propagating mode available to the system is differing only in the sine envelope, which is controlled by the parameter p, hence the subscript in Eq. (17). This formula can be reformulated into a matrix problem of the form $Ax = b$ for obtaining a quick numerical solution. The absorption cross section, which previously has been shown to be $1 - R$, with R being the reflectivity,[33] is calculated directly from the wave function ψ according to

$$\sigma = \frac{4\pi}{\lambda w} \int n_r(x,y)n_i(x,y)\psi(x,y)\,\mathrm{d}x\,\mathrm{d}y, \qquad (18)$$

where n_r and n_i are the real and imaginary parts of the complex index of refraction, respectively. In addition to Green's function method, the absorption cross section was also calculated using a commercial FDTD solver.[54] The wave function in Eq. (18) is then substituted with the electrical field obtained from the FDTD solver when the system reaches the steady state. Note that these programs differ in how the calculation is performed. In Green's function method, incoming waves with a correct shape according to Eq. (15) are injected into the bucket, while in the FDTD solver, a plane wave is sent toward a bucket with an infinite height. These two methods, however, yield approximately the same results since the incoming plane wave in the FDTD solver, once it hits the mirrors of the bucket, very quickly adjusts to the correct mirror boundary conditions. Matching the incoming plane wave with the modes (15) of the waveguide that leads to the dome, we obtain $\exp(-ik_y y) = \sum_q Z_q \exp(-ik_y y) \sin(q\pi x/w)$, where Z_q, $q = 1, 2, \ldots$, are the amplitudes of the waveguide modes excited by the incoming plane wave. Canceling $\exp(-ik_y y)$ on both sides, multiplying with $\sin(p\pi x/w)$, and integrating both sides over the interval $[0, w]$ yield $Z_p = 0$ for even p and $Z_p = 4/(\pi p)$ for odd p. This means that the main component excited by the incoming plane wave is $p = 1$ and the amplitudes of higher-order modes decrease according to $\sim 1/p$. Thus, since $Z_2 = 0$, the intensity of the lowest-p admixture, i.e., the $p = 3$ mode, is only about 10% of the $p = 1$ mode used as the incoming mode of our Green-function method and explains both the differences, but also the relatively good agreement between FDTD and our Green-function simulations. In fact, the incoming plane wave used by our FDTD solver is closer to reality since an incoming light wave is better modeled as a plane wave than as a

special mode of the type (15). This is so since compared to the wavelength of the incoming light, the waveguide leading to the dome is about ten times wider.

B. Computing the scattering matrix

For an incoming wave in mode p, the solution of the free problem is

$$\phi_p = (e^{-ik_y y} - e^{ik_y y}) \sin\left(\frac{p\pi x}{w}\right), \tag{19}$$

and we expect the scattered wave function to be a mixture of all possible waves allowed in the system, which is of the form

$$\psi_p = \sum_{m=1}^{M} S_{p\to m} \, e^{iB_m y} \sin\left(\frac{p\pi x}{w}\right) \tag{20}$$

in the asymptotic limit, i.e., $y \to \infty$. $S_{p\to m}$ denotes the scattering amplitude from the initial mode p to the final mode m. In this limit, the propagating-mode Green's function is

$$\lim_{y\to\infty} G_{prop} = G_{prop}^{(y\to\infty)} = \sum_{m=1}^{M} \frac{-2}{wB_m} \sin\left(\frac{m\pi x}{w}\right)$$

$$\times \sin\left(\frac{m\pi x'}{w}\right) e^{iB_m y} \sin(B_m y'). \tag{21}$$

Now, inserting $G_{prop}^{(y\to\infty)}$ into the Lippmann–Schwinger equation yields

$$\psi_p = \phi_p^{(y\to\infty)} + \int G_{prop}^{(y\to\infty)}(x, x', y, y') K^2$$

$$\times [1 - n(x', y')^2] \Psi_p(x', y') \, dx' \, dy' \tag{22}$$

from which, by comparing with Eq. (20), we can read off the scattering matrix elements

$$S_{p\to q} = -\delta_{pq} - \frac{2K^2}{wB_q} \int \sin\left(\frac{q\pi x'}{w}\right) \sin(B_q y')$$

$$\times [1 - n(x', y')^2] \psi_p(x', y') \, dx' \, dy'. \tag{23}$$

C. Enhancement of the absorption cross section

We calculated the absorption cross section according to Eq. (18) for the film+dome system as a function of the index of refraction, n_{dome}, for three film+dome systems. Figure 2 shows a comparison of the average absorption cross section $\langle\sigma\rangle_\lambda$, resulting from an average over a wavelength range spanning from 480 to 510 nm, between FDTD, $\langle\sigma_{FDTD}\rangle$, and Green's function method, $\langle\sigma_{GF}\rangle$. The Beer–Lambert efficiency, obtained from classical ray calculations, is also shown. These classical ray calculations were carried out using a ray-tracer software written specifically for the purpose of classical ray simulations. The details of the calculations can be found in Ref. 32. The FDTD and ray results agree very well. We expect this since the systems are close to the geometrical optics limit with the wavelengths being about ten times smaller than the total width of the systems. The $\langle\sigma_{GF}\rangle$ data are computed using the wave function of the first propagating mode, which has the form $e^{-ik_y y} \sin(k_x x)$. As discussed at the end of Sec. III A, the agreement
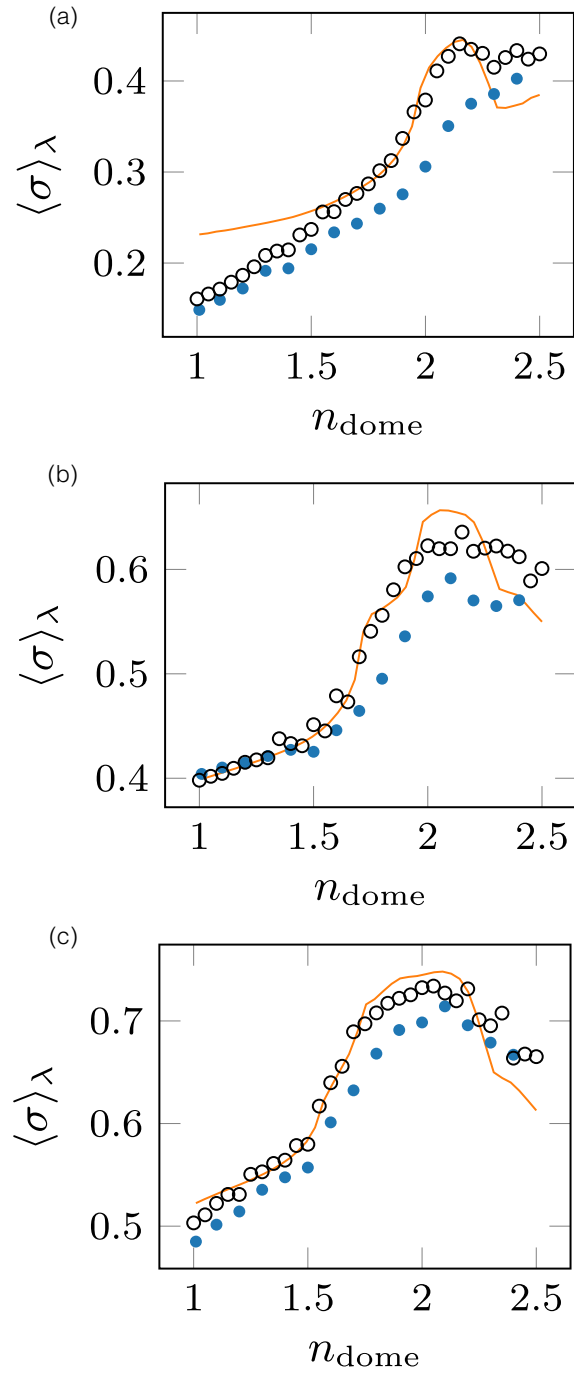

FIG. 2. Average absorption cross section $\langle\sigma\rangle_\lambda$, obtained by averaging $\sigma(\lambda)$ over a wavelength interval from 480 to 510 nm, calculated using FDTD (black circles) and Green's function approach (blue dots). Film thickness: (a) 1 μm, (b) 2 μm, and (c) 3 μm. For all three film thicknesses, a rapid increase in $\langle\sigma\rangle_\lambda$ is seen when n_{dome} is sufficiently large. The orange curve shows the efficiency calculated by geometric rays, including ray splitting, using Beer–Lambert's law to model absorption.[32]

with $\langle\sigma_{\text{FDTD}}\rangle$ is, therefore, not expected to be one-to-one since the incoming wave forms used in the two wave calculations (FDTD and Green's function method) are different. A plane wave is used in the FDTD calculation. However, the point here is not to make a direct comparison between the FDTD solver and Green's function calculations but to qualitatively search for the same behavior in $\langle\sigma\rangle_\lambda$ as a function of n_{dome} using rays, FDTD, and Green's function approach. The agreement between the full wave FDTD and the first-mode Green's function calculation is good despite the difference mentioned previously between the two programs.

All three models show an increase in the average absorption efficiency, $\langle\sigma\rangle_\lambda$, as n_{dome} is increased, with a maximum between 2.0 and 2.3. This holds true for all the systems with different film thicknesses. This shows that the maximum of the conversion efficiency occurs roughly at the index-matched situation, i.e., $n_{\text{dome}} \approx 2$ for all three film thicknesses. This is intuitively expected since a large index mismatch at the dome–film interface would lead to substantial reflection and a reduction in the conversion efficiency, an effect that is clearly visible in Fig. 2 for values of n_{dome} that are far away from $n = 2$. However, closer inspection of Fig. 2 also reveals that precise index matching is favorable only for thick films, whereas for thin films, the optimal n_{dome} may be different from the index-matched situation. For instance, in Fig. 2(a), corresponding to a thin film of film thickness $1\,\mu$m, we see that the maximum of efficiency occurs at $n_{\text{dome}} \approx 2.1$, i.e., higher than the index-matched situation, $n_{\text{dome}} = 2$. In Fig. 2(b), a thicker film of film thickness $2\,\mu$m, we see that the maximum moves to the left, toward $n_{\text{dome}} = 2$, but is still higher than the index-matched situation, i.e., $n_{\text{dome}} = 2$. In Fig. 2(c), which shows the conversion efficiency for yet a thicker film, at film thickness $3\,\mu$m, the maximum is now close to $n_{\text{dome}} = 2$, the index-matched situation. This corroborates the intuition that the index-matched situation is optimal for thick films, while for thin films, the optimal index of refraction may not be the index-matched situation. Of course, as we see in Fig. 2, the deviations from the index-matched situation will be small since, as mentioned above, a large index mismatch will lead to significant reflection, which reduces the conversion efficiency, as indeed observed in Fig. 2. Still, as we see in Fig. 2, even small changes in n_{dome} can have a significant effect on the efficiency: In Fig. 2(a), e.g., the difference in efficiency between the optimal n_{dome} and the index-matched n_{dome} is close to 5%.

We also observe that at a certain n_{dome}, $\langle\sigma\rangle_\lambda$ rapidly increases, hinting at a change of the dynamical behavior. This critical point is seen at about $n_{\text{dome}} = 1.85$, $n_{\text{dome}} = 1.6$, and $n_{\text{dome}} = 1.5$ for the systems with film thicknesses 1, 2, and $3\,\mu$m, respectively, with respect to the classical ray data (orange curve in Fig. 2). In other words, the phenomenon of the critical point with increasingly rapid enhancement of $\langle\sigma\rangle_\lambda$ is structurally stable; i.e., it does not depend on a strict choice of system parameters. However, the value of n_{dome} for which the critical point occurs does depend on the relative size difference of the film and dome. For instance, in the $1\,\mu$m thick film, the effect appears at a higher n_{dome} compared to the $3\,\mu$m thick film and is also stronger. This specific wavelength range, 480–510 nm, was chosen because it contains a significant part of the solar spectrum (including its maximum) while keeping the number of propagating modes available in the system [dictated by Eq. (14)], as large as possible. Care must be taken when calculating $\langle\sigma\rangle_\lambda$ over finite

wavelength intervals. The rule of thumb is that the interval must be broad enough to cover the average of σ to get a good agreement between the FDTD and classical ray calculations, which are not dependent on the wavelength in the same way as in FDTD. Using the $2\,\mu$m thick film as an example, we see, in Fig. 3(a), that roughly one "period" of σ is included in the chosen interval. Generally, σ is not expected to look periodic, but for small values of n_{dome}, the system is essentially just a film, which shows smooth, rolling fluctuations. One "period" of these fluctuations captures the average of σ. In Fig. 3(d), where n_{dome} is larger and σ is more packed with resonances, the calculated values are not so sensitive to the choice of the interval. There is a transition from slow [Figs. 3(a) and 3(b)] to rapid fluctuations [Figs. 3(c) and 3(d)], which hints at a change of the dynamics present in the scatterer. The high density of resonances we observe is also a feature of Ericson fluctuations, which are frequently associated with quantum chaotic scattering.[55,56] To prove that we are in the Ericson regime falls outside the scope of this paper. However, such an investigation would be of interest to the topic.

D. Signatures of chaos in the scattered wave function

In this section, we present evidence of chaos by inspecting the scattered wave functions visually. We look for two signatures of chaos in the distribution of the wave function field strength: scars[57] and scarlets.[58] These signatures provide straightforward and intuitive "litmus tests" to find whether chaos is present in a dynamical wave system or not. Scarlets are highly irregular patterns that manifest themselves as wrinkly filaments in the wave function field distribution arising in chaotic systems. Originally scarlets were discussed in the context of quantum chaos, but since then, experimental studies have shown the presence of scarlets in other wave systems such as acoustic resonators[59] and in water waves.[60] Thus, scarlets and scars are believed to be general wave phenomena. As we have come to expect for a chaotic system, Figs. 4(c) and 4(d) show scarlets in the wave function, while Figs. 4(a) and 4(b) show ordered patterns. This indicates that the scattering dynamics in the two latter cases are more regular than chaotic. These are strong indications that the film+dome system undergoes a transition from regular to chaotic scattering dynamics and is in agreement with the findings in Sec. III C.

Related to the work on eigenvalues and periodic-orbit theory by Gutzwiller,[61] Berry and Tabor,[48,62] and Balian and Bloch,[63] Heller[57] found that unstable periodic orbits have a very visible effect on the eigenfunctions of classically chaotic systems. In some wave functions, the classical path of the periodic orbits can be seen directly in cases where the fluctuations in the wave function have a higher density along the path. Figure 5 shows two wave functions that are scarred by periodic orbits. In Fig. 5(b), a triangular orbit is scarring the wave function. This scarring surrounds a periodic orbit of a similar shape. Additionally, the phase space contains periodic orbits that zig-zag across the x axis, such as the one shown in Fig. 5(d). From a ray-trapping perspective, the existence of such orbits can be very important. The rays move in an almost horizontal fashion, resulting in a long path length in the absorbing film. This motion is very desirable in light-trapping schemes. However, the periodic rays of a scattering system cannot be reached by rays coming from outside of
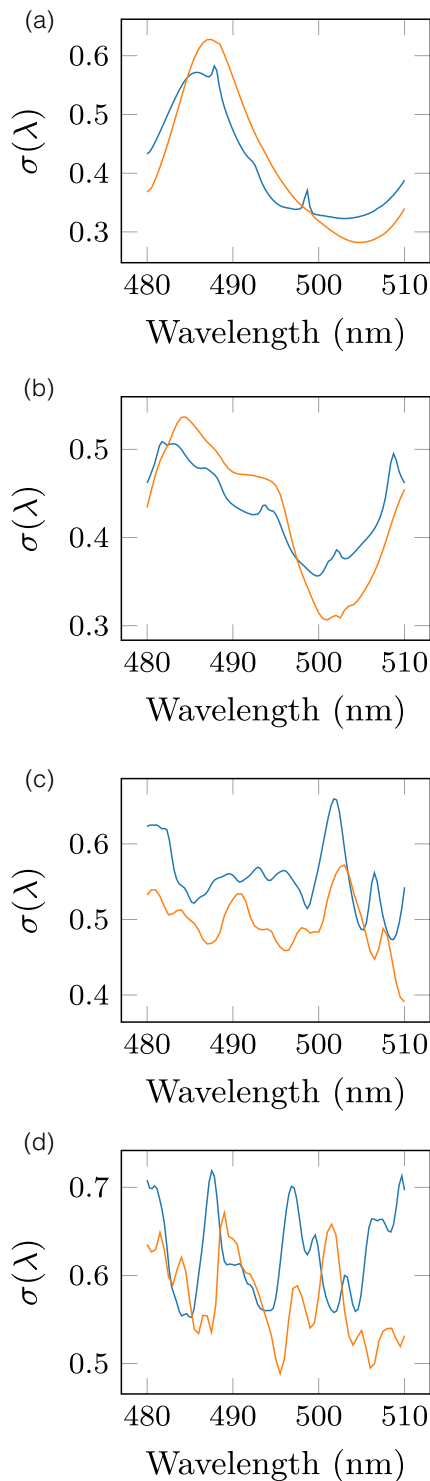
FIG. 3. Comparison of the spectral absorption cross section as calculated by FDTD (blue) and the first propagating mode from Green's function approach (orange). (a) $n_{dome} = 1.2$, (b) $n_{dome} = 1.4$, (c) $n_{dome} = 1.8$, (d) $n_{dome} = 2.0$.

the scatterer, but they can get arbitrarily close, thus being effectively trapped considering their finite lifetimes due to absorption.

An arrow-shaped pattern can be seen in Fig. 4(b), which resembles a scar. An orbit undergoing a total internal reflection at that angle is not possible for $n_{dome} = 1.2$. These scar-like patterns are due to ray splitting, i.e., rays that split into a reflected and transmitted component at the boundary at the air–dome interface.

E. Transition to chaotic scattering dynamics

Assuming the Bohigas–Giannoni–Schmit conjecture, the distribution of the nearest-neighbor spacings, $P(s)$, of the eigenangles of the eigenvalues $e^{i\xi}$ of the S matrix are universal. We will now look closely at these distributions for the film+dome system as a function of n_{dome}.

When the dome is completely removed from the film+dome model, the system is fully integrable and an analytic closed-form solution can easily be found. An integrable scattering system has fully regular scattering dynamics with uncorrelated levels, which follow Poissonian statistics; see Fig. 6(a). In Fig. 6(b), we see that a depression at small s appears. Placing the dome structure on top of the film destroys the integrability of the system, even with a very low index of refraction $n_{dome} = 1.01$. For values of n_{dome} close to 1, the system is said to be pseudo-integrable. In this case, the system has no classically chaotic counterpart, and there is no global universality for $P(s)$ to explain the shape of the distribution.[64] At $n_{dome} = 1.1$ and $n_{dome} = 1.2$, the level distribution is clearly not a Poissonian but has not fully developed into a Wigner distribution either. There is level repulsion shown in the distributions, but the peak is skewed to the left of what the Wigner surmise predicts.

In the event where an integrable system is perturbed, a smooth transition to mixed dynamics is expected.[44,65,66] This is contrary to the abrupt transition to chaos of an integrable Hamiltonian that is made ergodic.[64] We expect our system to be the former. It is, therefore, difficult to see the onset of chaos by visually comparing the distributions with the Wigner surmise. We apply an objective statistical test to quantify exactly where the transition from regular to chaotic dynamics occurs. The χ^2 goodness of fit test, which we used, is described in more detail in Sec. B.

The χ^2 test shows the probability of obtaining a histogram that gives a higher χ^2 value when compared to a certain distribution. Lower χ^2 values are better. Both the Berry–Robnik distribution and the Brody distribution were used in the χ^2 test against the histograms of the level statistics. By varying the "chaoticity parameters," $\bar{\rho}$ and ω, for the Berry–Robnik and Brody distributions, respectively, in the interval [0, 1], we find the best-fitting distributions. Figure 7 shows histograms of level spacing distributions as n_{dome} is increased in steps of 0.1. The best-fitting Berry–Robnik and Brody distributions are plotted on top of the histograms. The level statistics were gathered for wavelengths in the intervals 457–474 nm and 477–497 nm for a total of 3129 nearest-neighbor level spacings for the film thickness 2 μm. For the 1 and 3 μm thick films, only the interval 477–497 nm with 1620 nearest-neighbor level spacings were used.

First, by visually inspecting Fig. 7, we see that the Berry–Robnik and Brody distributions start to fit better to the histograms for $n_{dome} = 1.6$ and higher, indicating that the onset of chaos starts

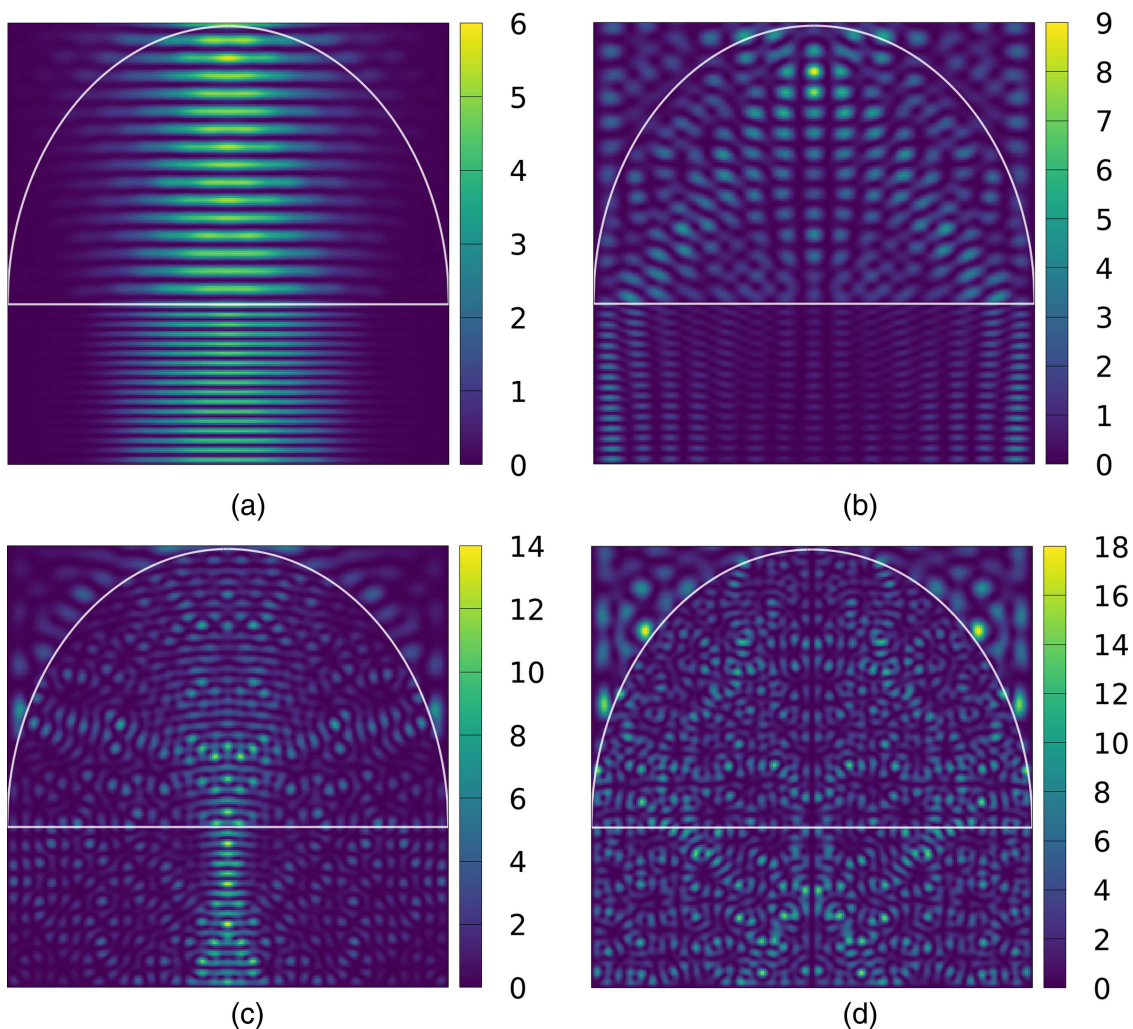**FIG. 4.** Irregularities in the scattered wave function become more and more prevalent with increasing n_{dome}. This is a signature of chaos. (a) $n_{dome} = 1.1$, (b) $n_{dome} = 1.2$, (c) $n_{dome} = 1.8$, (d) $n_{dome} = 2.0$.

around this value. There are statistical fluctuations present in the level statistics histograms due to the sample size and the size of the S matrices. We assume that a histogram agrees well with the distribution it is compared to if the probability is higher than some limit. If the probability is lower than the limit, the deviation from the distribution is said to be statistically significant. We chose to use 5% as the limit in our statistical tests. Figure 8 shows the probabilities obtained from the χ^2 test for each value of n_{dome}. The smooth transition of the level statistics from an integrable system (no dome), to the pseudo-integrable, to chaotic, makes it difficult for the histograms to pass strictly the statistical test we apply. We, therefore, expect only the cases with well-developed chaos to pass the test. The test is passed for n_{dome} values 1.9, 1.6, 1.5 (passing values), and above for the film+dome systems with 1, 2, and 3 μm thick films, respectively. However, due to the statistical fluctuations present, there are

some outliers. The passing values match closely with the critical points 1.85, 1.6, 1.5 for the 1 μm, 2 μm and 3 μm thick films, respectively, which are the n_{dome} values where a rapid enhancement of the absorption cross section is observed.

F. Chaos enhanced light trapping

The autocorrelation function of an S-matrix element is defined as

$$\mathcal{A}(\lambda) = \frac{\int \tilde{S}_{i,j}^*(\lambda)\tilde{S}_{i,j}(\lambda + \Delta\lambda)\,\mathrm{d}\lambda}{\int \tilde{S}_{i,j}^*(\lambda)\tilde{S}_{i,j}(\lambda)\,\mathrm{d}\lambda}, \qquad (24)$$

where $\tilde{S}_{i,j}(\lambda)$ is the fluctuating part of the S-matrix element $S_{i,j}$; i.e., the mean background is removed. It measures the correlation of the
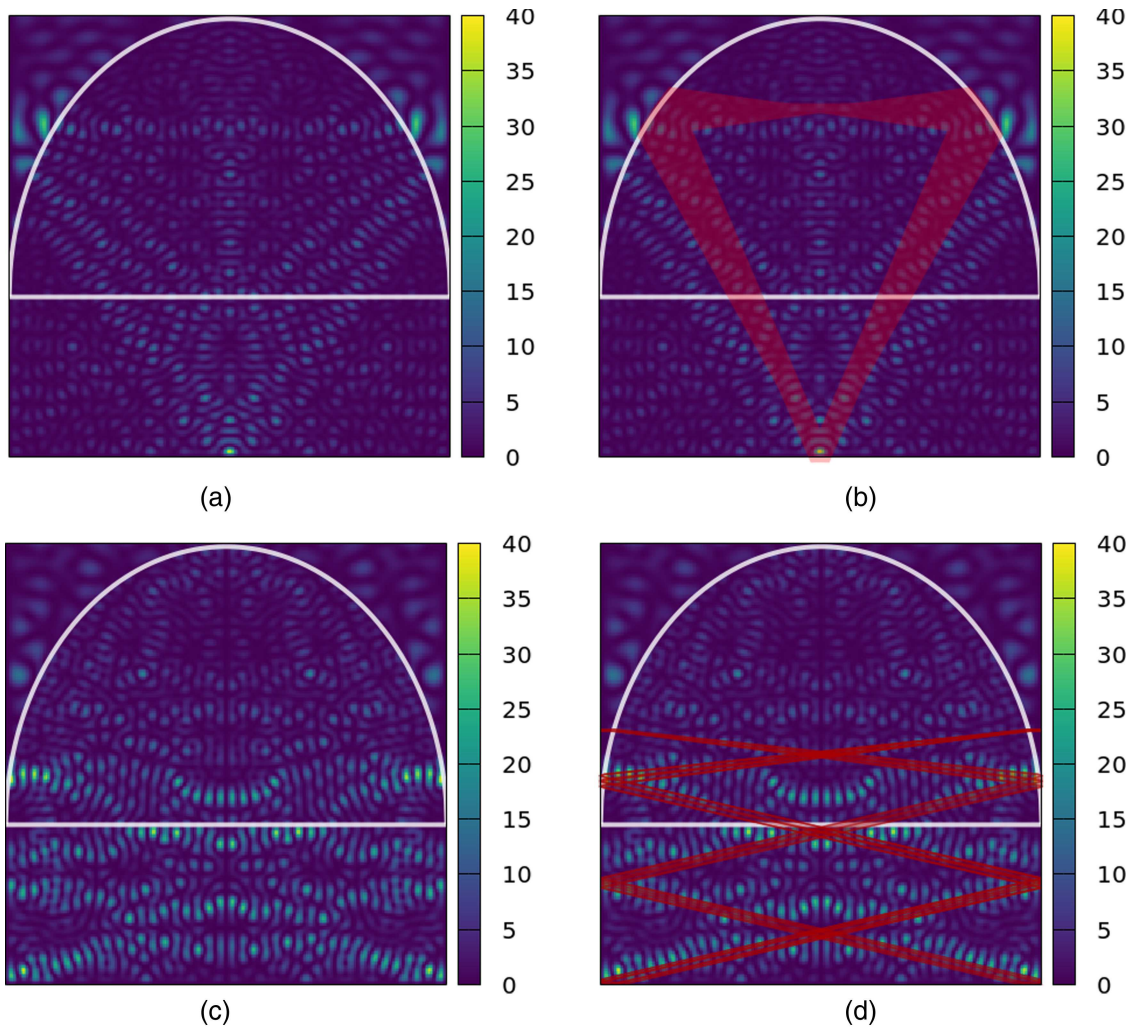
FIG. 5. (a) and (c) show scars in the scattered wave function, which trace the path of a periodic orbit. In (b) and (d), the scarred orbits are superposed. The two examples are from the film+dome system with a 1 μm thick film and $n_{\text{dome}} = 2.0$.

S-matrix elements as a function of the wavelength of the incoming wave, λ. The half-width at half-maximum of the autocorrelation function in energy is inversely proportional to the classical lifetime τ of rays,[55]

$$\tau = \frac{1}{v\Delta k},\qquad (25)$$

where v is the speed and

$$\Delta k = \frac{2\pi}{\lambda^2}\Delta\lambda.\qquad (26)$$

Thus, from (25), we get an approximation of the lifetime of the rays, $\langle L_{\mathcal{A}}\rangle$, in the classically analog systems to the quantum film+dome system. Using the 2 μm thick film+dome system as an example, we subtract the mean background from the scattering matrix.

Then, (24) can be used to calculate the autocorrelation function $\mathcal{A}$ as a function of $\Delta\lambda$. This analysis was done in three different ways: (1) using the $S_{2,1}$ element of the even-parity S matrix of the film+dome system, (2) averaging over 16 off-diagonal S-matrix elements, and (3) averaging over all diagonal S-matrix elements [see open orange, green, and blue circles in Fig. 9(a), respectively]. The analysis was done for each value of n_{dome}. The autocorrelation functions are shown in Fig. 9(b). By tracing 10000 non-Newtonian rays (NNR), the average geometric path length for the classical rays, $\langle L_{\text{NNR}}^{\text{geo}}\rangle$, was also computed [see the solid blue line in Fig. 9(a)]. Non-Newtonian rays can split into a transmitted and reflected ray for each encounter with a ray-splitting boundary with the appropriate probability weights according to the Fresnel equations. As a consequence, the trajectories propagate through the film+dome scatterer and split such that their probability goes toward zero. The
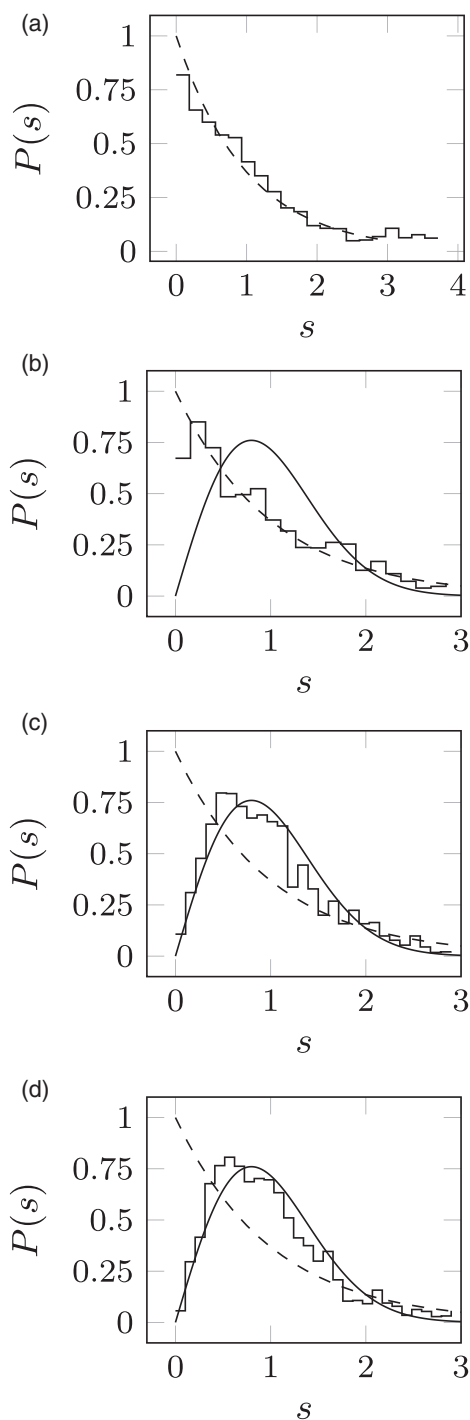
FIG. 6. The dashed line is the Poisson distribution, $P(s) = e^s$, and the solid line is the Wigner surmise. For low values of n_{dome}, the film+dome system is pseudo-integrable. At n_{dome} equal to 1.1 and 1.2, the distributions are between the pseudo-integrable and Wigner case. (a) No dome, (b) $n_{dome} = 1.01$, (c) $n_{dome} = 1.1$, (d) $n_{dome} = 1.2$.

average path lengths computed from the autocorrelation functions, $\langle L_{\mathcal{A}} \rangle$, and classical rays, $\langle L_{NNR}^{geo} \rangle$, are increasing as a function of n_{dome}, and they are shown in Fig. 9(a). There is remarkably good agreement between the classical ray calculations and the quantum wave calculations.

The connection between experimentally optimizing light trapping by surface structures and the results presented here is the average path length of rays. Knowing how the average path length of rays depends on various system parameters is very useful, but the average path length cannot be measured directly. However, as we have seen, it can be extracted from the autocorrelation function, which can be measured. Thus, the fact that the autocorrelation function can be measured experimentally[25] makes it a powerful diagnostic tool that can be used to optimize the light-trapping capabilities of new surface-structure designs.

G. Relevance for realistic systems

In this section, we discuss the relevance of our results for light trapping in realistic solar cells. We do this in three stages. In Sec. III G 1, we show that considering the realistic case of anti-reflection coatings and encasing solar-cell components in a protective film, the index of refraction chosen up to now in this paper for our simulations, i.e., $n \approx 2$, is already a realistic choice for several high-performance solar-cell materials, including silicon. In Sec. III G 2, we then show that even without protective layers, our choice of $n \approx 2$ is realistic since it can be applied directly to inorganic, inorganic–organic, or organic solar-cell materials of current interest that naturally have $n \approx 2$. In Sec. III G 3, presenting the results of additional classical simulations, we show explicitly that our methods can be applied to solar-cell materials of higher indexes of refraction and that our conclusions derived from the cases with $n \approx 2$ still hold. Thus, we show that our methods are relevant for optimizing the light-trapping efficiency of solar cells no matter what specific energy-converting material is used, ranging from a low index of refraction inorganic, inorganic–organic, and organic materials to high-performance inorganic materials with large indexes of refraction. In addition, our additional simulations for different indexes of refraction, presented in Sec. III G 3, support our claim that even without access to high-performance computational hardware (a laptop computer is sufficient), the necessary simulations are efficient and can easily be repeated for many different choices of indexes of refraction, surface-structure geometries, and film thicknesses.

1. Front layers

It is well known in optics that in the case of geometric ray optics, where diffraction phenomena are absent, the absolute values of refractive indexes do not matter; all that matters is their *ratios* when transitioning from one material to another.[14] Therefore, if a silicon solar cell with $n \approx 4$ is covered with a transparent film or an anti-reflection coating with index of refraction $n \approx 2$ (for instance, silicon nitride, SiN_x, whose index of refraction is tunable from 1.6 to 2.7, has a near-zero absorption coefficient, and is widely used on silicon solar cells as antireflection coating[67]), then our classical ray simulations, performed for the case of $n \approx 2$ in both dome structures and films, are directly relevant to this case since the ratio of $n \approx 4$
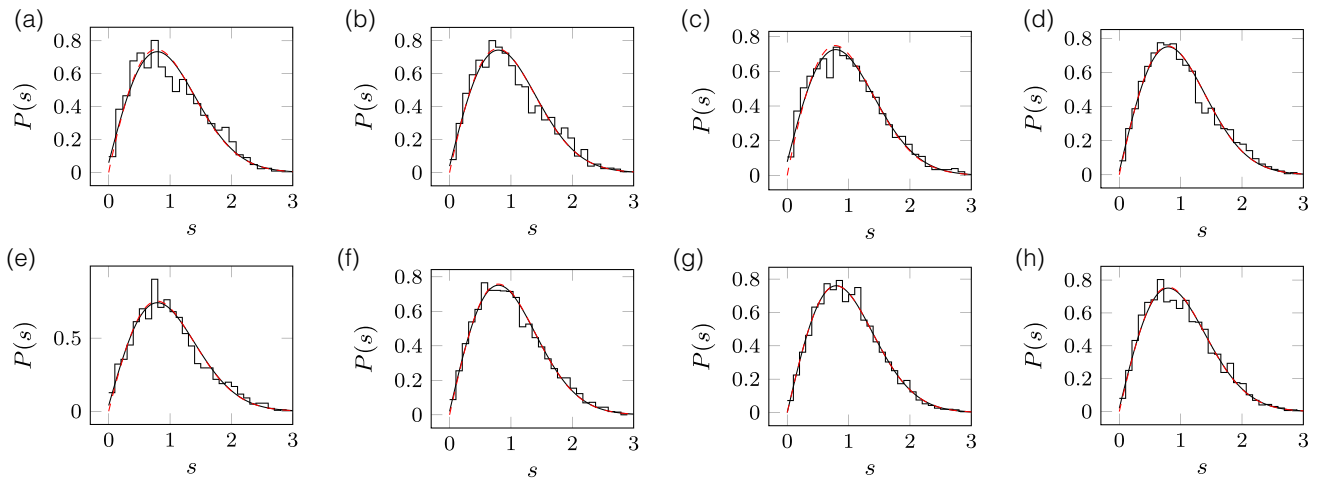
FIG. 7. The histograms show the level statistics of the different film+dome systems. The smooth black line is the best-fitting Berry–Robnik distribution, and the red dashed line is the best-fitting Brody distribution. (a) $n_{dome} = 1.3$, (b) $n_{dome} = 1.4$, (c) $n_{dome} = 1.5$, (d) $n_{dome} = 1.6$, (e) $n_{dome} = 1.7$, (f) $n_{dome} = 1.8$, (g) $n_{dome} = 1.9$, (h) $n_{dome} = 2.0$.

inside the dome+film system and $n \approx 2$ outside the dome+film system is about 2, i.e., the same values that were used in our classical simulations. We emphasize that all realistic solar-cells in an actual practical use are encased in some kind of protective material, which always lowers the effective index of refraction. Thus, our classical simulations above, while not focused on a specific solar-cell material, are nevertheless already performed in an index of refraction regime that is in the range of realistic inorganic solar-cell materials. We show in Sec. III G 2 that realistic solar-cell materials exist, which
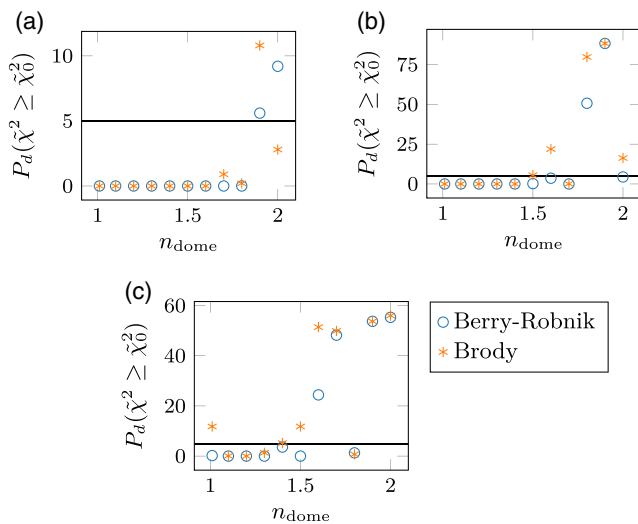

FIG. 8. P_d is the probability of finding a $\tilde{\chi}^2$ higher than $\tilde{\chi}_0^2$, which corresponds to the best fit. The 5% limit is shown as a horizontal line. The best-fitting Berry–Robnik and Brody distributions are found by maximizing P_d. Film thickness: (a) 1 μm, (b) 2 μm, and (c) 3 μm.
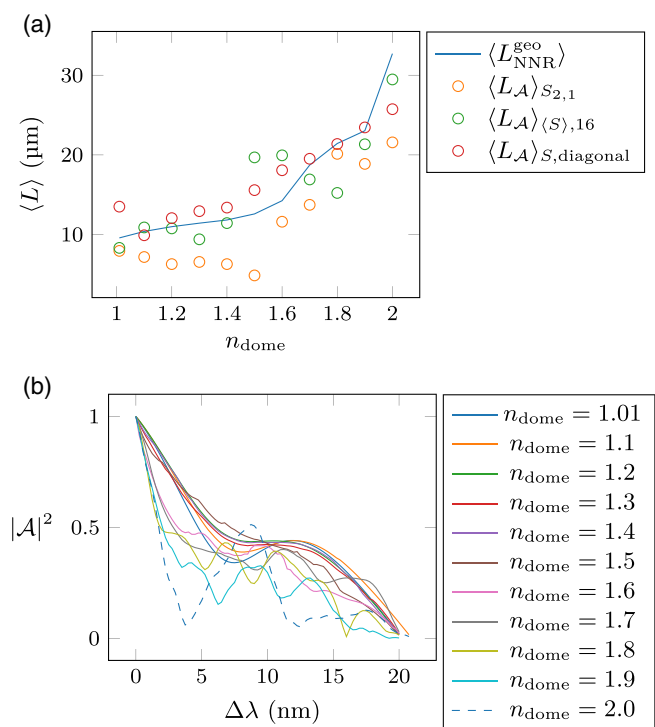

FIG. 9. (a) The average geometric path length, calculated by ray-tracing 10 000 non-Newtonian rays (blue full line), derived from the width of the autocorrelation function, using $S_{2,1}$ (orange open circles), using an average over 16 off-diagonal S-matrix elements (green open circles), and averaging over all diagonal S-matrix elements (red open circles). (b) Autocorrelation function, $|\mathcal{A}(\lambda)|^2$, of $\tilde{S}_{2,4}$. The half-width at half-maximum decreases as n_{dome} increases. This correlates the transition to chaotic dynamics with longer classical path lengths present in the system.

naturally have indexes of refraction around $n \approx 2$. For those materials, even without coverings, our simulations, performed above with $n \approx 2$, are of direct relevance.

2. Solar-cell materials with $\Re(n) \approx 2$

There is a large class of solar-cell materials with $n \approx 2$. These can be grouped loosely into inorganic, inorganic–organic, and organic solar-cell materials.[68] While not yet as efficient as silicon as energy-conversion materials, these materials have recently surfaced as serious contenders for the construction of solar cells because of their desirable material properties, e.g., ease of manufacture or pliability. Typical representatives of the inorganic, inorganic–organic, and organic families of solar-cell materials are, e.g., $CsPbBr_3$,[69] the perovskite $CH_3NH_3PbI_3$,[70] and C60,[71] with $n \approx 1.9$, 2.2, and 2.1, respectively, in the spectral region around $\lambda \approx 500$ nm. While these substances have n in the range used in our simulations above, the imaginary parts of their indexes of refraction are considerably larger than what we used in our simulations. However, since we use the imaginary part of the index of refraction only as a probe of the effectiveness of light trapping and since the imaginary part of the index of refraction does not influence the transition to chaos, it is unimportant for our optimization mechanism. The existence of realistic solar-cell materials with real parts of the index of refraction in the range of our simulations above demonstrates that our simulations are realistic. To remove any doubt about the applicability of our method to realistic systems, we present in Subsection III G 3 the case of silicon, which demonstrates that our method works for the most popular solar-cell material where we also chose exactly the index of refraction, both real and imaginary parts, as they apply to silicon.
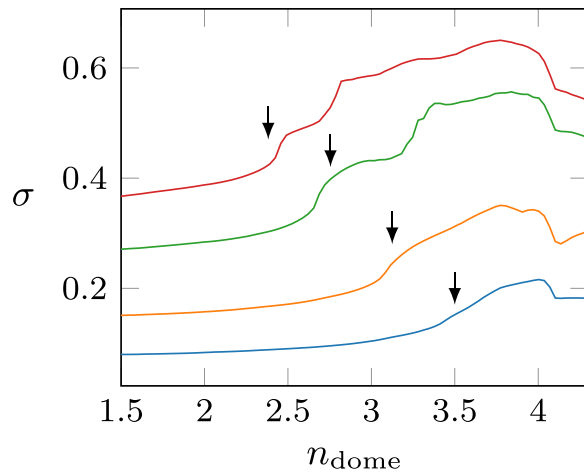
FIG. 10. The absorption cross section obtained by non-Newtonian rays incident on the dome+film system for film thicknesses 0.5 μm (blue), 1.0 μm (orange), 2 μm (green), and 3 μm (red). The arrows show the value of n_{dome} where Newtonian rays have a sudden surge in path length (Fig. 11). This is an indication of the onset of chaotic dynamics in the system.
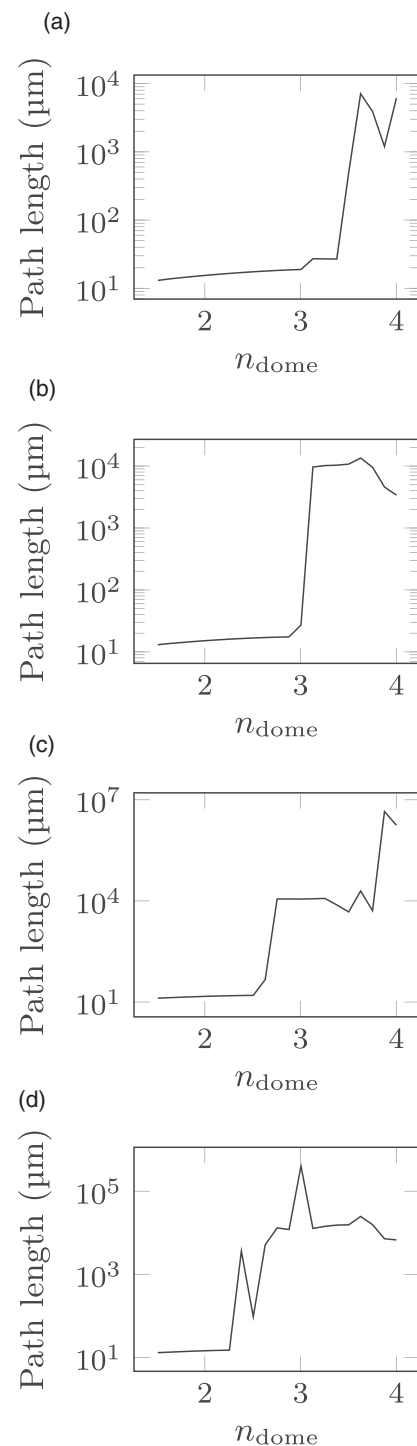
FIG. 11. The maximal lifetime of Newtonian rays sent orthogonally into the system with respect to the film–dome interface, expressed as path length. The sudden surge in the maximal path length is an indication that the system is becoming chaotic. Film thickness: (a) 0.5 μm, (b) 1.0 μm, and (c) 2.0 μm, (d) 3.0 μm.

3. Silicon

In this section, we present a realistic thin-film solar-cell system consisting of a Si film as the energy-conversion material, a dome as a surface structure, and a protective coating with index of refraction $n = 1.5$. Since the most challenging spectral region for thin-film technology is in the red or infrared spectral regions, where Si has a very small absorption efficiency and light trapping becomes of great importance, we chose for our demonstration Si at 800 nm with refractive index $n = 3.675 + 0.0054i$.[72]

Figure 10 shows the result of the conversion efficiency for four different film thicknesses as a function of n_{dome}. As expected on the basis of the discussion in Sec. III G 1, we see the same phenomena emerging as already observed in our simulations with $n \approx 2$; i.e., (i) the onset of strong conversion efficiency coincides with the onset of chaos (arrows in Fig. 10) and (ii) the efficiency curves shift to the left for increased film thickness.

For each film thickness, the onset of chaos was determined by looking for a jump in the lifetime of rays as a function of n_{dome}. This is justified since the onset of chaotic scattering is accompanied by the emergence of the scattering fractal, which contains rays of infinite lifetime. As demonstrated in Fig. 11, the transition to very large lifetimes is sharp, which means that the onset of chaos can be unambiguously extracted from Fig. 11. The arrows in Fig. 10 are placed at those values of n_{dome} where the sharp transition to long-lifetime rays occurs in Fig. 11.

Thus, we established, using the exact Si index of refraction, both real and imaginary parts, that our basic conclusion about the tight connection between light-trapping efficiency and chaos stays valid, even in the case of realistic inorganic solar-cell materials with a large index of refraction.

IV. CONCLUSIONS

We have observed the existence of a critical region in n_{dome} where the absorption cross section starts to increase rapidly in a solar cell model with a light-trapping surface structure. By changing the index of refraction in the light-trapping structure, the scattering dynamics of the system makes a transition from regular scattering to the irregular, chaotic scattering regime at a critical value of n_{dome}. We show that there is a three-way correlation between the onset of chaotic scattering, the increase of the path length of rays in the scatterer, and the increase of the absorption cross section.

The implications are of substantial importance. Researchers in laboratories and industry are already making thinner solar cells to improve voltage characteristics and lowering the cost, but the lowered efficiency that comes with thin solar cells is a major obstacle, which, to be overcome, demands smart management of light. The three-way correlation shows that chaos can be used as a design guide for computationally prototyping surface structures. All the tools needed to evaluate a given structure and the degree of chaos it induces in a system are readily available. By measuring the autocorrelation function presented, the increase in the average path length can be verified experimentally.

In this paper, using both classical ray-tracing and E&M wave simulations, we established a new, fundamental mechanism in solar-cell optimization, i.e., chaos-induced enhancement of conversion efficiency. Due to the fundamental nature of our findings, we have no doubt that our results will be of use for the design of highly efficient surface-structured thin-film solar cells.

APPENDIX A: GREEN'S FUNCTION APPROACH TO SOLVING THE HELMHOLTZ EQUATION

We solve the Helmholtz equation

$$(\nabla^2 + n^2 K^2)\psi = 0 \tag{A1}$$

by using Green's function method. To construct Green's function, we choose eigenfunctions that satisfy the boundary conditions, which are defined by our model system. The model is defined as a 2D region where $x \in [0, w]$ and $y \in [0, \infty]$ such that

$$\psi(x, 0) = 0, \tag{A2a}$$

$$\psi(0, y) = \psi(w, y). \tag{A2b}$$

We choose eigenfunctions of the form

$$\phi_{mk}(x, y) = \mathcal{N}_{mk} \sin\left(\frac{m\pi x}{w}\right)\sin(ky), \tag{A3}$$

where $k \in \mathbb{R}$, $m \in \mathbb{I}$ is the mode index and $\mathcal{N}_{mk}$ are the normalization constants.

The eigenfunctions are normalized,

$$\int_0^w \int_0^\infty \phi_{mk}(x, y)\phi_{m'k'}(x, y)^* \, dx\, dy = 1, \tag{A4}$$

$$\mathcal{N}_{mk}\mathcal{N}_{m'k'} \int_0^w \int_0^\infty \sin\left(\frac{m\pi x}{w}\right)\sin\left(\frac{m'\pi x}{w}\right)$$
$$\times \sin(ky)\sin(k'y)\, dx\, dy = 1. \tag{A5}$$

We can do the integrals separately

$$\int_0^\infty \sin(ky)\sin(k'y)\, dy = \frac{\pi}{2}\delta(k - k'). \tag{A6}$$

The integral

$$\int_0^w \sin\left(\frac{m\pi x}{w}\right)\sin\left(\frac{m'\pi x}{w}\right) dx \tag{A7}$$

or, equivalently,

$$-\frac{1}{2}\int_0^w \left[\cos\left((m + m')\frac{\pi x}{w}\right) - \cos\left((m - m')\frac{\pi x}{w}\right)\right] dx \tag{A8}$$

can be split into two cases,

$$\frac{1}{2}\int_0^w 1\, dx = \frac{w}{2}, \quad m = m', \tag{A9}$$

$$-\frac{1}{2}\int_0^w \left[\cos\left((m+m')\frac{\pi x}{w}\right) - \cos\left((m-m')\frac{\pi x}{w}\right)\right] dx = 0,$$

$$m \neq m'. \tag{A10}$$

With $m = m'$ and $k = k'$, the two normalization integrals give

$$\mathcal{N}_{mk} = \frac{2}{\sqrt{\pi w}}; \tag{A11}$$

thus, the eigenfunctions are

$$\boxed{\phi_{mk}(x,y) = \frac{2}{\sqrt{\pi w}} \sin\left(\frac{m\pi x}{w}\right) \sin(ky).} \tag{A12}$$

Green's function is defined as

$$\mathcal{D}_{xy} G(x,x',y,y';K) = \delta(x-x')\delta(y-y'), \tag{A13}$$

where the 2D operator $\mathcal{D}_{xy}$ is

$$\mathcal{D}_{xy} = \frac{\partial^2}{\partial x^2} + \frac{\partial^2}{\partial y^2} + K^2. \tag{A14}$$

We can expand Green's function in terms of the eigenfunctions $\phi_{mk}(x,y)$

$$G(x,x',y,y';K) = \sum_{m=-\infty}^{\infty} \int_0^{\infty} c_{mk}(x',y')\phi_{mk}(x,y)\, dk \tag{A15}$$

and find the expansion coefficients $c_{mk}(x',y')$ by doing

$$\mathcal{D}_{xy} G(x,x',y,y';K) = \delta(x-x')\delta(y-y'), \tag{A16}$$

$$\mathcal{D}_{xy} \sum_{m=-\infty}^{\infty} \int_0^{\infty} c_{mk}(x',y')\phi_{mk}(x,y)\, dk = \delta(x-x')\delta(y-y'). \tag{A17}$$

$\mathcal{D}_{xy}$ only operates on ϕ_{mk}; therefore, we get

$$\mathcal{D}_{xy}\phi_{mk}(x,y) = \phi_{mk}(x,y)\left(K^2 - \frac{\pi^2 m^2}{w^2} - k^2\right). \tag{A18}$$

Before we insert into (A17), we rewrite the delta functions

$$\delta(x-x') = \frac{2}{w}\sum_{m=1}^{\infty} \sin\left(\frac{m\pi x}{w}\right) \sin\left(\frac{m\pi x'}{w}\right), \tag{A19}$$

$$\delta(y-y') = \frac{2}{\pi}\int_0^{\infty} \sin(ky)\sin(ky')\, dk. \tag{A20}$$

Now, (A17) has the form

$$\sum_{m=-\infty}^{\infty} \int_0^{\infty} c_{mk}(x',y')\phi_{mk}(x,y)\left(K^2 - \frac{\pi^2 m^2}{w^2} - k^2\right) dk$$

$$= \frac{4}{\pi w}\sum_{m=-\infty}^{\infty} \sin\left(\frac{m\pi x}{w}\right) \sin\left(\frac{m\pi x'}{w}\right) \int_0^{\infty} \sin(ky)\sin(ky')\, dk, \tag{A21}$$

and we see directly that

$$c_{mk}(x',y') = \frac{\phi_{mk}(x',y')}{K^2 - \frac{\pi^2 m^2}{w^2} - k^2}. \tag{A22}$$

We arrive at the bilinear form of G

$$G(x,x',y,y';K) = \sum_{m=-\infty}^{\infty} \int_0^{\infty} \frac{\phi_{mk}(x,y)\phi_{mk}(x',y')\, dk}{K^2 - \frac{\pi^2 m^2}{w^2} - k^2}. \tag{A23}$$

Next, we carry out the integral where only the y-dependent part of G contains k; thus, the integral we need to consider is

$$\int_0^{\infty} \frac{\sin(ky)\sin(ky')\, dk}{K^2 - \frac{\pi^2 m^2}{w^2} - k^2 + i\epsilon}, \tag{A24}$$

where the $i\epsilon$ is an infinitesimal size added to do the complex integration. Two cases must be considered,

$$K^2 - \frac{\pi^2 m^2}{w^2} > 0 \quad \text{for propagating modes}, \tag{A25}$$

$$K^2 - \frac{\pi^2 m^2}{w^2} < 0 \quad \text{for evanescent modes}. \tag{A26}$$

We let

$$A_m = \sqrt{\frac{\pi^2 m^2}{w^2} - K^2}, \tag{A27}$$

$$B_m = \sqrt{K^2 - \frac{\pi^2 m^2}{w^2}}. \tag{A28}$$

Since $2\sin(ky)\sin(ky') = \cos[k(y-y')] - \cos[k(y+y')]$, we only consider the following integrals for the case of propagating modes:

$$\int_0^{\infty} \frac{\cos[k(y-y')]\, dk}{B_m^2 - k^2 + i\epsilon} = -\frac{\pi i}{2B_m}e^{iB_m|y-y'|}, \tag{A29}$$

$$-\int_0^{\infty} \frac{\cos[k(y+y')]\, dk}{B_m^2 - k^2 + i\epsilon} = -\frac{\pi i}{2B_m}e^{iB_m(y+y')} \tag{A30}$$

and the following for the case of evanescent modes:

$$\int_0^{\infty} \frac{\cos[k(y-y')]\, dk}{-A_m^2 - k^2} = -\frac{\pi}{2A_m}e^{-A_m|y-y'|}, \tag{A31}$$

$$-\int_0^{\infty} \frac{\cos[k(y+y')]\, dk}{-A_m^2 - k^2 + i\epsilon} = -\frac{\pi}{2A_m}e^{-A_m(y+y')}. \tag{A32}$$

The number of propagating modes, M, is decided by the summation index m. From Eq. (A25), we get

$$M = \left\lfloor \frac{Kw}{\pi} \right\rfloor. \tag{A33}$$

Now, we can write down the complete expression for Green's function,

$$
\begin{aligned}
G_{prop} &= \sum_{m=1}^{M} \frac{i}{wB_m} \sin\left(\frac{m\pi x}{w}\right) \sin\left(\frac{m\pi x'}{w}\right) \\
&\quad \times \left[e^{iB_m(y+y')} - e^{iB_m|y-y'|} \right], \\
G_{eva} &= \sum_{m=M+1}^{\infty} \frac{1}{wA_m} \sin\left(\frac{m\pi x}{w}\right) \sin\left(\frac{m\pi x'}{w}\right) \\
&\quad \times \left[e^{-A_m(y+y')} - e^{-A_m|y-y'|} \right].
\end{aligned} \tag{A34}
$$

APPENDIX B: BINNING AND THE χ^2 GOODNESS OF FIT TEST

The χ^2 goodness of fit test was performed as described in Taylor's book *An Introduction to Error Analysis*.[73] For our purposes, eigenangles were extracted from the S-matrix samples and then binned before applying the χ^2 test. The bin width was determined using the Freedman–Diaconis rule;[74] i.e., the bin width is dependent on N, the size of the data set. The Freedman–Diaconis bin width b_w is defined as

$$
b_w = \frac{2\mathrm{IQR}}{\sqrt[3]{N}}, \tag{B1}
$$

where IQR is the interquartile range of the data set.

χ^2 is a measure of the agreement between an observed distribution O_k and an expected distribution E_k. It is defined as

$$
\chi^2 = \sum_{k=1}^{N} \frac{(O_k - E_k)^2}{E_k}. \tag{B2}
$$

In the unlikely event that there is a perfect agreement, χ^2 will be 0. However, if the fit is good, it is expected that χ^2 will be on the same order as N or smaller. If the fit is bad, χ^2 will be much larger than N. In order to say something about the quality of the fit, we look at how likely it is to find some value χ_0^2 for a given data set and expected distribution. Specifically, we calculate the probability for finding a χ^2 greater than the χ_0^2 found from the data. This probability is given as

$$
Prob_d(\tilde{\chi}^2 \geq \tilde{\chi}_0^2) = \frac{2}{2^{d/2}\Gamma(d/2)} \int_{\chi_0}^{\infty} x^{d-1} e^{-x^2/2} \, dx, \tag{B3}
$$

where d is the number of degrees of freedom, $d = N - c$, the number of observations minus the number of constraints. $\tilde{\chi}^2 = \chi^2/d$ is called the reduced chi squared.

DATA AVAILABILITY

The data that support the findings of this study are available from the corresponding author upon reasonable request.

REFERENCES

[1] International Energy Agency, see http://www.iea-pvps.org/index.php?id=266 for "IEA: A Snapshot of Global PV"; accessed 5 August 2019.

[2] T. Tiedje, E. Yablonovitch, G. D. Cody, and B. G. Brooks, "Limiting efficiency of silicon solar cells," IEEE Trans. Electron Devices **31**, 711–716 (1984).

[3] L. C. Andreani, A. Bozzola, P. Kowalczewski, M. Liscidini, and L. Redorici, "Silicon solar cells: Toward the efficiency limits," Adv. Phys.: X **4**, 1548305 (2019).

[4] M. A. Green, Y. Hishikawa, E. D. Dunlop, D. H. Levi, J. Hohl-Ebinger, and A. W. Ho-Baillie, "Solar cell efficiency tables (version 51)," Prog. Photovoltaics Res. Appl. **26**, 3–12 (2018).

[5] K. Yoshikawa, H. Kawasaki, W. Yoshida, T. Irie, K. Konishi, K. Nakano, T. Uto, D. Adachi, M. Kanematsu, H. Uzu, and K. Yamamoto, "Silicon heterojunction solar cell with interdigitated back contacts for a photoconversion efficiency over 26%," Nat. Energy **2**, 17032 (2017).

[6] J. Gjessing, E. S. Marstein, and A. Sudbø, "2D back-side diffraction grating for improved light trapping in thin silicon solar cells," Opt. Express **18**, 5481–5495 (2010).

[7] J. Gjessing, A. Sudbø, and E. Marstein, "A novel back-side light-trapping structure for thin silicon solar cells," J. Eur. Opt. Soc. Rapid Publ. **6**, 11020 (2011).

[8] C. Battaglia, C.-M. Hsu, K. Söderström, J. Escarré, F.-J. Haug, M. Charrière, M. Boccard, M. Despeisse, D. T. L. Alexander, M. Cantoni, Y. Cui, and C. Ballif, "Light trapping in solar cells: Can periodic beat random?," ACS Nano **6**, 2790–2797 (2012).

[9] P. Kowalczewski, M. Liscidini, and L. C. Andreani, "Light trapping in thin-film solar cells with randomly rough and hybrid textures," Opt. Express **21**, A808–A820 (2013).

[10] Q. Tang, H. Shen, H. Yao, K. Gao, Y. Jiang, Y. Li, Y. Liu, L. Zhang, Z. Ni, and Q. Wei, "Superiority of random inverted nanopyramid as efficient light trapping structure in ultrathin flexible C-Si solar cell," Renew. Energy **133**, 883–892 (2019).

[11] Y. Xu and Y. Xuan, "Photon management of full-spectrum solar energy through integrated honeycomb/cone nanostructures," Opt. Commun. **430**, 440–449 (2019).

[12] J. Grandidier, D. M. Callahan, J. N. Munday, and H. A. Atwater, "Light absorption enhancement in thin-film solar cells using whispering gallery modes in dielectric nanospheres," Adv. Mater. **23**, 1272–1276 (2011).

[13] H. A. Atwater and A. Polman, "Plasmonics for improved photovoltaic devices," Nat. Mater. **9**, 205 (2010).

[14] F. L. Pedrotti, L. M. Pedrotti, and L. S. Pedrotti, *Introduction to Optics*, 3rd ed. (Pearson Education, Inc., 2007).

[15] J. M. Seoane and M. A. F. Sanjuán, "New developments in classical chaotic scattering," Rep. Prog. Phys. **76**, 016001 (2012).

[16] E. Ott and T. Tél, "Chaotic scattering: An introduction," Chaos **3**, 417–426 (1993).

[17] R. Blümel and W. P. Reinhardt, *Chaos in Atomic Physics* (Cambridge University Press, 1997).

[18] P. Cvitanović, R. Artuso, R. Mainieri, G. Tanner, and G. Vattay, *Chaos: Classical and Quantum* (Niels Bohr Institute, Copenhagen, 2016).

[19] A. Kohler and R. Blümel, "Annular ray-splitting billiard," Phys. Lett. A **238**, 271–277 (1998).

[20] A. Kohler and R. Blümel, "Signature of periodic lateral-ray orbits in a rectangular ray-splitting billiard," Phys. Lett. A **247**, 87–92 (1998).

[21] A. Kohler and R. Blümel, "Test of semiclassical amplitudes for quantum ray-splitting systems," Phys. Rev. E **59**, 7228–7230 (1999).

[22] A. Kohler, G. H. M. Killesreiter, and R. Blümel, "Ray splitting in a class of chaotic triangular step billiards," Phys. Rev. E **56**, 2691–2701 (1997).

[23] A. Kohler and R. Blümel, "Weyl formulas for quantum ray-splitting billiards," Ann. Phys. **267**, 249–280 (1998).

[24] N. Savytskyy, A. Kohler, S. Bauch, R. Blümel, and L. Sirko, "Parametric correlations of the energy levels of ray-splitting billiards," Phys. Rev. E **64**, 036211 (2001).

[25] Y. Hlushchuk, A. Kohler, S. Bauch, L. Sirko, R. Blümel, M. Barth, and H.-J. Stöckmann, "Autocorrelation function of level velocities for ray-splitting billiards," Phys. Rev. E **61**, 366–370 (2000).

[26] L. P. Kadanoff and C. Tang, "Escape from strange repellers," Proc. Natl. Acad. Sci. U.S.A. **81**, 1276–1279 (1984).

[27] P. Gaspard and S. A. Rice, "Scattering from a classically chaotic repellor," J. Chem. Phys. **90**, 2225–2241 (1989).

[28] L. A. Bunimovich, "On the ergodic properties of nowhere dispersing billiards," Commun. Math. Phys. **65**, 295–312 (1979).

[29]L. A. Bunimovich, "On ergodic properties of certain billiards," Funct. Anal. Appl. **8**, 254–255 (1974).

[30]E. Yablonovitch, "Statistical ray optics," J. Opt. Soc. Am. **72**, 899–907 (1982).

[31]M. Mariano, G. Kozyreff, L. G. Gerling, P. Romero-Gomez, J. Puigdollers, J. Bravo-Abad, and J. Martorell, "Intermittent chaos for ergodic light trapping in a photonic fiber plate," Light Sci. Appl. **5**, e16216 (2016).

[32]E. Seim, A. Kohler, R. Lukacs, M. A. Brandsrud, E. S. Marstein, E. Olsen, and R. Blümel, "Chaos: A new mechanism for enhancing the optical generation rate in optically thin solar cells," Chaos **29**, 093132 (2019).

[33]M. Brandsrud, E. Seim, R. Lukacs, A. Kohler, E. Marstein, E. Olsen, and R. Blümel, "Exact ray theory for the calculation of the optical generation rate in optically thin solar cells," Physica E **105**, 125–138 (2019).

[34]N. Chernov and R. Markarian, *Chaotic Billiards* (American Mathematical Society, 2006).

[35]G. Gallavotti, "Lectures on the billiard," in *Dynamical Systems, Theory and Applications: Battelle Seattle 1974 Rencontres* (Springer, Berlin, 1975), Chap. 7, pp. 236–295.

[36]F. Haake, *Quantum Signatures of Chaos*, 3rd ed. (Springer, Berlin, 2010).

[37]E. P. Wigner, "Characteristic vectors of bordered matrices with infinite dimensions," Ann. Math. **62**, 548–564 (1955).

[38]A. M. Lane, R. G. Thomas, and E. P. Wigner, "Giant resonance interpretation of the nucleon-nucleus interaction," Phys. Rev. **98**, 693–701 (1955).

[39]M. L. Mehta, *Random Matrices and the Statistical Theory of Energy Levels*, 2nd ed. (Academic Press, 1991).

[40]M. V. Berry, "Classical chaos and quantum eigenvalues," in *Order and Chaos in Nonlinear Physical Systems* (Springer US, Boston, MA, 1988), Chap. 11, pp. 341–348.

[41]M. L. Mehta and J. Des Cloizeaux, "The probabilities for several consecutive eigenvalues of a random matrix," Ind. J. Pure Appl. Math. **3**, 329–351 (1972).

[42]O. Bohigas, M. J. Giannoni, and C. Schmit, "Characterization of chaotic quantum spectra and universality of level fluctuation laws," Phys. Rev. Lett. **52**, 1–4 (1984).

[43]H.-J. Stökmann, *Quantum Chaos: An Introduction* (Cambridge University Press, Cambridge, 2000).

[44]D. Wintgen and H. Friedrich, "Classical and quantum-mechanical transition between regularity and irregularity in a Hamiltonian system," Phys. Rev. A **35**, 1464–1466 (1987).

[45]M. V. Berry, M. Tabor, and J. M. Ziman, "Level clustering in the regular spectrum," Proc. R. Soc. London, Ser. A **356**, 375–394 (1977).

[46]G. Casati, B. Chirikov, and I. Guarneri, "Energy-level statistics of integrable quantum systems," Phys. Rev. Lett. **54**, 1350 (1985).

[47]S. W. McDonald and A. N. Kaufman, "Spectrum and eigenfunctions for a Hamiltonian with stochastic trajectories," Phys. Rev. Lett. **42**, 1189–1191 (1979).

[48]M. Berry, "Quantizing a classically ergodic system: Sinai's billiard and the KKR method," Ann. Phys. **131**, 163–216 (1981).

[49]M. Robnik, "The energy level statistics of Hamiltonian systems between integrability and chaos: The semiclassical limit," Math. Comput. Simul. **40**, 159–179 (1996).

[50]M. V. Berry and M. Robnik, "Semiclassical level spacings when regular and chaotic orbits coexist," J. Phys. A: Math. Gen. **17**, 2413 (1984).

[51]T. A. Brody, "A statistical measure for the repulsion of energy levels," Lett. Nuovo Cimento (1971-1985) **7**, 482–484 (1973).

[52]T. A. Brody, J. Flores, J. B. French, P. A. Mello, A. Pandey, and S. S. M. Wong, "Random-matrix physics: Spectrum and strength fluctuations," Rev. Mod. Phys. **53**, 385–479 (1981).

[53]J. D. Jackson, *Classical Electrodynamics* (Wiley, New York, 1999).

[54]Lumerical, Inc., see www.lumerical.com for "FDTD Solutions," 2019.

[55]R. Blümel and U. Smilansky, "Classical irregular scattering and its quantum-mechanical implications," Phys. Rev. Lett. **60**, 477–480 (1988).

[56]R. Blümel and U. Smilansky, "A simple model for chaotic scattering: II. Quantum mechanical theory," Physica D **36**, 111–136 (1989).

[57]E. J. Heller, "Bound-state eigenfunctions of classically chaotic Hamiltonian systems: Scars of periodic orbits," Phys. Rev. Lett. **53**, 1515–1518 (1984).

[58]P. O'Connor, J. Gehlen, and E. J. Heller, "Properties of random superpositions of plane waves," Phys. Rev. Lett. **58**, 1296–1299 (1987).

[59]P. A. Chinnery and V. F. Humphrey, "Experimental visualization of acoustic resonances within a stadium-shaped cavity," Phys. Rev. E **53**, 272 (1996).

[60]R. Blümel, I. Davidson, W. Reinhardt, H. Lin, and M. Sharnoff, "Quasilinear ridge structures in water surface waves," Phys. Rev. A **45**, 2641 (1992).

[61]M. C. Gutzwiller, "Periodic orbits and classical quantization conditions," J. Math. Phys. **12**, 343–358 (1971).

[62]M. V. Berry, M. Tabor, and J. M. Ziman, "Closed orbits and the regular bound spectrum," Proc. R. Soc. London, Ser. A **349**, 101–123 (1976).

[63]R. Balian and C. Bloch, "Solution of the Schrödinger equation in terms of classical paths," Ann. Phys. **85**, 514–545 (1974).

[64]M. Robnik, "A note on the level spacings distribution of the Hamiltonians in the transition region between integrability and chaos," J. Phys. A: Math. Gen. **20**, L495–L502 (1987).

[65]M. Robnik, "Quantising a generic family of billiards with analytic boundaries," J. Phys. A: Math. Gen. **17**, 1049–1074 (1984).

[66]H.-D. Meyer, E. Haller, H. Koppel, and L. S. Cederbaum, "On the connection between irregular trajectories and the distribution of quantum level spacings," J. Phys. A: Math. Gen. **17**, L831–L836 (1984).

[67]T. Iwahashi, M. Morishima, T. Fujibayashi, R. Yang, J. Lin, and D. Matsunaga, "Silicon nitride anti-reflection coating on the glass and transparent conductive oxide interface for thin film solar cells and modules," J. Appl. Phys. **118**, 145302 (2015).

[68]*Spectroscopic Ellipsometry for Photovoltaics Volume 1: Fundamental Principles and Solar Cell Characterization*, Springer Series in Optical Sciences Vol. 212, edited by H. Fujiwara and R. W. Collins (Springer, Cham, 2018).

[69]H. Yuan, Y. Zhao, J. Duan, Y. Wang, X. Yang, and Q. Tang, "All-inorganic $CsPbBr_3$ perovskite solar cell with 10.26% efficiency by spectra engineering," J. Mater. Chem. A **6**, 24324–24329 (2018).

[70]P. Löper, M. Stuckelberger, B. Niesen, J. Werner, M. Filipic, S.-J. Moon, J.-H. Yum, M. Topic, S. De Wolf, and C. Ballif, "Complex refractive index spectra of $CH_3NH_3PbI_3$ perovskite thin films determined by spectroscopic ellipsometry and spectrophotometry," J. Phys. Chem. Lett. **6**, 66–71 (2015).

[71]D. Wynands, M. Erber, R. Rentenberger, M. Levichkova, K. Walzer, K.-J. Eichhorn, and M. Stamm, "Spectroscopic ellipsometry characterization of vacuum-deposited organic films for the application in organic solar cells," Org. Electron. **13**, 885–893 (2012).

[72]M. A. Green, "Self-consistent optical parameters of intrinsic silicon at 300 K including temperature coefficients," Sol. Energy Mater. Sol. Cells **92**, 1305–1310 (2008).

[73]J. R. Taylor, *An Introduction to Error Analysis: The Study of Uncertainties in Physical Measurements* (University Science Books, 1997).

[74]D. Freedman and P. Diaconis, "On the histogram as a density estimator: L2 theory," Z. Wahrscheinlichkeitstheorie Verw. Geb. **57**, 453–476 (1981).